In-operando observation of microstructural evolution in a solid oxide cell electrolyte operating at high polarization

Sierra, J. X.; Poulsen, H. F.; Jørgensen, P. S.; Detlefs, C.; Cook, P.; Simons, H.; Jakobsen, A. C.; Bowen, J. R.

Published in:
Journal of Power Sources

Link to article, DOI:
10.1016/j.jpowsour.2018.12.057

Publication date:
2019

Document Version
Peer reviewed version

In-operando observation of microstructural evolution in a solid oxide cell electrolyte operating at high polarization

*J. X. Sierra[a], H. F. Poulsen[b], P. S. Jørgensen[a], C. Detlefs[c], P. Cook[c], H. Simons[b], A. C. Jakobsen[b], J. R. Bowen[*a]*

[a] *Department of Energy Conversion and Storage, Technical University of Denmark, Frederiksborgvej 399, 4000 Roskilde, Denmark*

[b] *Department of Physics, Technical University of Denmark, Anker Engelunds Vej 1 Bygning 101A, 2800 Kgs. Lyngby*

[c] *European Synchrotron Radiation Facility, 71 Avenue des Martyrs, 38000 Grenoble, France*

Abstract

In the present work a symmetric scandia yttria stablilized zirconia electrolyte based solid oxide cell is investigated *in-operando* by synchrotron X-ray diffraction as a function of time and position within the electrolyte while annealing at 700°C in air and at a polarization of 2V. In addition, scanning electron microscopy experiments are carried out on similar cells operating at temperatures of 700, 800 and 900°C. Void formation in the grain boundaries of the electrolyte close to the anode/electrolyte interface is detected as early as 6 hours. No clear trend is observed with respect to cell operation time and temperature in cells with equal grain size. However, grain boundary surface area may be inversely related to the frequency of void observations. A decrease of d-spacing in the anode interface region can be attributed to compressive stress associated with oxygen pressure build up. Decrease of d-spacing in the cathode/electrolyte region could be associated to oxide ion deficiency. Dark field X-ray microscopy is used to map for the first time the strain gradients within an electrolyte grain close to the anode region. Changes in strain domains after 10.5 hours at operating conditions are assumed to be associated with early stages of void formation.

Keywords: solid oxide cell; strain; x-ray diffraction; grain boundary; nanoscale void formation

[*] Corresponding author: Jacob R. Bowen, jrbo@dtu.dk, +45 21 32 83 84

1. Introduction

Solid oxide cells (SOCs) have acquired increasing interest in energy production and storage applications because of their exceptional electrochemical and physical properties. SOCs can operate efficiently in two modes. In fuel cell mode (solid oxide fuel cell: SOFC) electrical energy is produced by electrochemical reactions involving oxygen and fuel (hydrogen and/or hydrocarbons), while in electrolysis mode (solid oxide electrolysis cell: SOEC) oxygen and hydrogen are produced from steam and/or carbon monoxide and oxygen from carbon dioxide, giving the possibility to store the chemicals for later energy production or chemical synthesis (1) (2) (3).

Due to the electrochemical reactions and the high operating temperature, SOCs exhibit degradation phenomena, which are detrimental to the cells performance and lifetime. In long-term experiments (on the order of hundreds to thousands of hours) severe degradation occurs under high current densities.

Knibbe et al. (4) discovered intergranular and transgranular fractures running along the yttria stabilized zirconia (YSZ) grain boundaries and the formation of pores in the grain boundaries of an YSZ electrolyte based cell. The fuel and oxygen electrodes, which are also known as cathode and anode respectively when running in electrolysis mode, consisted of Ni/YSZ and strontium doped lanthanum manganite/YSZ (LSM/YSZ) and the cell was tested at 850 °C for 188 hours under a current density of -2 A/cm^2. It was concluded that the porosity is formed during operation at high current density. Energy dispersive X-ray spectroscopy (EDS) revealed the composition of the entrapped gas to be mainly oxygen. Similar pore formations and transgranular fractures were observed by Tietz et al. (5) after 9000 hours at a current density of -1 A/cm^2 in micrographs of fractured surfaces. The cell consisted of an 8%mol-YSZ electrolyte and a porous diffusion barrier layer of gadolinia doped ceria (CGO) with lanthanum strontium cobalt ferrite (LSCF) and Ni/YSZ as the oxygen and fuel electrodes respectively. Sun et al. (6) reported cracks, detachment and cavities close to the anode interface by scanning electron microscopy (SEM) in the polished cross section of cells with similar electrode/electrolyte composition as in Knibbe et al. (4) after 900 hours at 850 °C and -1.5 A/cm^2. Graves et al. (2) observed nanosized pores in YSZ electrolyte grain boundaries of a cell composed of Ni/YSZ and LSM/YSZ electrodes, by scanning transmission electron microscopy, after 420 hours in electrolysis mode at 800 °C and -1 A/cm^2.

It is suggested that this formation of porosity in the grain boundaries of the electrolyte close to the electrolyte/oxygen electrode interface is due to an increase in oxygen activity, caused by the distribution of the electromotive potential and resulting in a high internal oxygen pressure build up

in this region (4) (7) (8). An oxygen partial pressure on the order of 10 MPa has been proposed by Virkar (9), based on brittle materials properties, to cause delamination of the anode at typical temperatures of 800 °C. Therefore, we expect the high oxygen pressure to result in compressive stresses and thus a reduction of electrolyte lattice parameter close to the anode interface.

In order to increase the efficiency of the cell, YSZ electrolytes are commonly co-doped with scandia ($Sc_2O_3 - Y_2O_3 - Zr_2O_3$, ScYSZ) as ScYSZ provides a larger ionic conductivity than YSZ for equivalent temperature (10) (11). Thus, reduction of operating temperatures by 100-200°C is enabled. This in turn improves the degradation behavior of other SOC stack components and reduces mechanical issues associated with thermal expansion mismatches and chemical instabilities (12) (13) (14). To our knowledge, pore formation as observed above in YSZ electrolytes has not been reported for scandia-yttria stabilized zirconia electrolytes in electrolysis mode.

Resolving the cause of the void formation has been hampered by a lack of methods to directly observe the microstructure evolution at the nanometer scale, within the relevant deeply embedded region and during operation of the cell. Thus, here we take advantage of recent advances in synchrotron X-ray diffraction techniques to present a novel in-operando investigation of microstructure evolution within the bulk of ScYSZ electrolyte based symmetrical SOC under high polarization. Changes in lattice parameter across the cell are determined by local X-ray diffraction as a function of depth from electrode interfaces and dark field X-ray microscopy (DFXRM) (15) (16) is used to map internal strain gradients within individual electrolyte grains.

2. Experimental

2.1. Cell design

Symmetric cells were produced with the electrolyte consisting of $(Y_2O_3)_{0.01}(Sc_2O_3)_{0.10}(ZrO_2)_{0.89}$ (henceforth denoted ScYSZ) provided by Daiichi Kigenso Kagaku Kogyo Co., LTD. Prepared by tape casting these have an approximate thickness of 180 µm. One half of the ScYSZ sheet was thermally treated at 1600 ˚C for 1 hour and the other half was left with no thermal treatment. The larger grains of the thermally treated samples allows studying the size dependency of the void formation and results in a suitable grain size for the *in-operando* synchrotron experiments. A 50/50% slurry of LSM/YSZ was sprayed on both sides of each sheet as electrodes, thereby creating a symmetrical cell, suitable for testing at high temperature in air. The cells were then sintered at 600 ˚C for 4 hours and 1300 ˚C for 6 hours, with a cooling rate of 60˚C/hour, achieving an electrode thickness of 5-10 µm. Rectangular pieces with dimensions specified in the following sections were

cut using a diamond blade wheel (Minitom, Struers A/S). To ensure electronic conductivity, platinum cables with a 2 mm flattened tip were bonded to the electrodes with platinum paste. To hold all components together an Aron Ceramic, class D inorganic adhesive paste was used. Approximately half of the cell was left exposed to the furnace air atmosphere as the active part.

Two types of experiments were performed. 1) Void statistics experiments, where cells were tested for a specific duration and condition after which their internal structure was examined. 2) *In-operando*, where the structure of grains was probed over time with synchrotron X-rays. A similar sample setup was utilized for both types of experiments primarily dictated by the constraints of the synchrotron experiment, i.e. small cell size, large grain size, atmospheric air gas environment and high polarization to accelerate degradation processes to be detectable within the beamtime duration.

2.2. Void statistics experiments

Samples with dimensions 1.6x5 mm^2 were tested in atmospheric air at 700, 800, and 900 $^{\circ}$C. A fixed potential of 2V was applied for durations of 6 to 48 hours and 6 to 72 hours for thermally treated and non-thermally treated ScYSZ electrolyte based cells respectively. The experiments were carried out in an alumina tube furnace and the cells were placed at a maximum of 15 mm from the thermocouple. The cells were then fractured *post-mortem* close to the interface of the active region and the ceramic paste to perform scanning electron microscopy (SEM) (see §2.4 for details).

According to this configuration, the cell acts as an electrochemical oxygen pump. Oxygen reduction occurs at the cathode/electrolyte interface, oxide ions then conduct through the electrolyte driven by the potential difference at the electrodes, reaching the anode where they are released as oxygen molecules. The overall equation is given by:

$$\text{(cathode)}\ \ O_2 + 4e^- \rightarrow 2O^{2-} \rightarrow O_2 + 4e^-\ \text{(anode)} \qquad \text{Eq. 1}$$ *(17) (18)*

2.3. In-operando experiment

2.3.1. Cell characterization

The *in-operando* cell was made using the same procedure as described in the cell design but with dimension 0.33x4x0.18 mm, (see Figure S1 in supplementary material) in directions "x", "y" and "z" respectively, with reference to the coordinate system in **Error! Reference source not found.**.

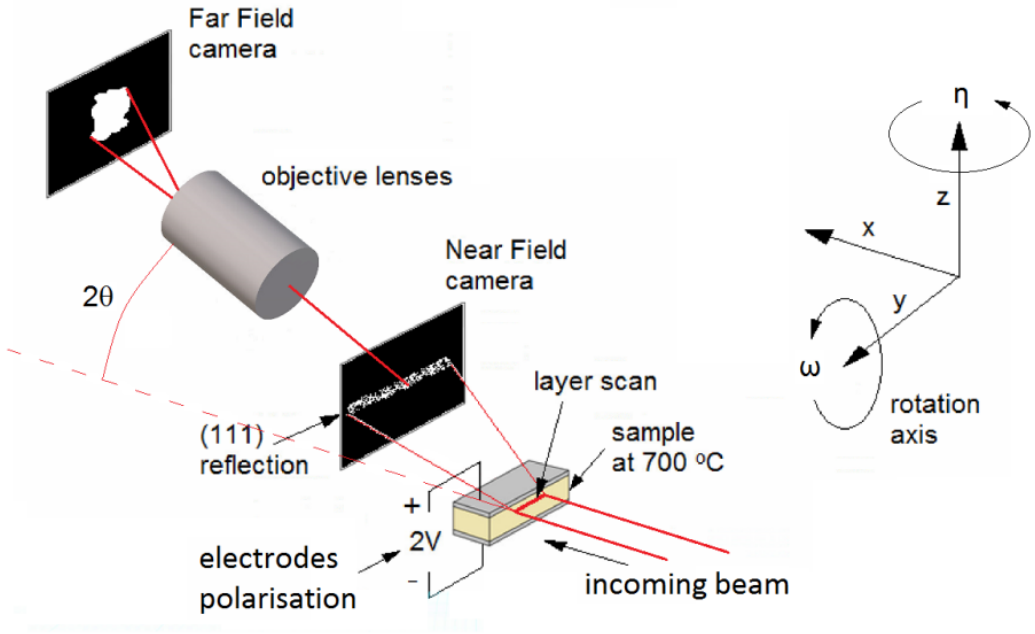

Figure 1. Schematic view of the sample setup at beamline ID06 (furnace is not included). The near field camera can be translated out of the diffracted beam enabling dark field microscopy by means of an X-ray objective.

The experiment took place at the ESRF beamline ID06 using 17 keV X-rays. The cross section of the incident beam was defined by a silicon condenser – a compound refractive lens – with a resulting FWHM of 350x17 µm in "y" and "z" directions respectively. The cell was electrochemically operated (*in-operando*) in air at 700 °C for a total of 32 hours. It was scanned repeatedly with respect to the beam in the "z" direction in 51 steps covering a range of 0.25 mm, henceforth referred to as a layer scan. The top and bottom of the cell were identified from the absence of the diffracted signal outside the sample. The experimental geometry is sketched in Figure 1. The goniometer allows rotations around both the y- and z-axis. The diffraction signal from ScYSZ (111) was studied using alternately a near field camera and a dark field microscope using a far field camera.

A hot air gas blower with a nominal maximum temperature of 1000 °C was used to provide the high temperature to the cell. The temperature was raised from room temperature to the maximum in approximately 5 hours. Due to the limitations of the furnace-detector geometry, the sample was placed a few millimeters away from the hottest part of the furnace, to allow detection of the (111) diffraction line. Thus, the temperature of the sample was 700 °C, estimated by a thermocouple placed approximately 2 mm away from the sample. The temperature calibration was done as follows. First, the thermocouple was placed in analogous position of the cell by using the same sample holder. Second, the thermocouple was moved 2 mm away to allow the temperature difference to be measured. Finally, the *in-operando* experiment temperature was estimated considering that difference previously measured with the thermocouple at 2 mm from the cell.

After the temperature had stabilized at 700 °C the voltage was set to 2.0 V across the cell. The time of the last layer scan performed was 24.7 h after applying the voltage and the total exposure time at operating conditions was 32 hours. Collection of diffraction data after the 24.7 h measurement was not experimentally possible due to failure in the data acquisition system.

During the high temperature part of the experiment five stages were defined as follows, excluding the room temperature stage as the starting point of the experiment:

- 0V: no applied voltage
- XXh@2V: applied voltage of 2V for XX hours. XX values are: 0.0, 2.4, 17.0 and 24.7.

After the *in-operando* experiment void formation was investigated by post-mortem SEM on fractured and polished cross-sections (see §2.4).

2.3.2. Near field set-up

The *near field set-up* involves a FreLoN camera coupled to a scintillator screen, with a resulting effective pixel size of 0.622 μm and 2048x2048 pixels. Placed at a distance of 50 mm from the sample in "x", a segment of the (111) Debye-Scherrer ring is observed. An example of a raw image can be seen in Figure S2 in the supplementary material. The grains in the illuminated volume give rise to distinct diffraction spots. These are sampled while performing a continuous scan in ω, with a range of 4° in steps of 0.01°. From the center-of-mass position of the spots on the detector we can derive statistics of grain average properties, in particular grain volume, and the average axial strain within a grain (19). From the width of the peaks in the y-direction on the detector and in angle ω, we can determine the mosaic spread of the associated grain.

The near field data was analyzed using the program: "peaksearch" in Fable (20). A background was subtracted from all images. This was defined for each pixel as the median value over 10 subsequent images. The filtering rejected peaks with less than 5 pixels, saturated pixels, and peaks

associated with low integrated intensity and a mosaicity lower than twice the ω step, in order to remove noise and uncertainties in the center of mass position in the images. The average d-spacing of the (111) was estimated by the positions of the filtered peaks in the "Z" direction of the near field images at all "ω" of each layer.

2.3.3. Dark field set-up

The *dark field microscope set-up* allows mapping of the structure and strain within selected grains. A compound refractive lens composed of 70 beryllium lenses was placed between the sample and the detector. Suitably aligned this acts as an objective, magnifying the projection of a given grain by 16 times. The far field camera was a FreLoN camera coupled to a scintillator screen, with a resulting effective pixel size of 1.4 μm and 2048x2048 pixels. The resulting theoretical spatial resolution of the dark field set-up was approximately 300 nm (21). By tilting the sample in ω and η within the estimated mosaicity range, maps can be made of the orientation gradient within the grain. By scanning the scattering angle 2θ (see Figure 1) the local axial strain component is probed (21). To integrate over the rocking curve during acquisition in such a strain scan the sample was continuously rotated (rocked) over a ±0.05 range in ω. The data analysis followed the procedure presented by Ahl et al. (22).

2.4. Electron microscopy

A Carl Zeiss SUPRA-35 Gemini FEGSEM scanning electron microscope at an accelerating voltage of 2kV was used to observe the morphology of the *post-mortem* fractured sample using the secondary electron detector SE2 (Everhart-Thornley). The approximate width of images was 20.5 μm.

Polished cross-sections were also imagined at 2kV and EDS analysis was carried out at 29 kV to avoid yttrium and zirconium *k*-alpha peak overlap using a ThermoFisher Noran System 6 EDS detector.

3. Results

The measure of the average electrolyte grain size was determined by the linear intercept length method (23) from five SEM images of separated sections of each bulk sample, after applying thermal etching at 1400 °C for 10 minutes, giving 6.3±1.8 and 12.8±4.1 μm (±1 standard deviation) for pristine and thermally treated ScYSZ electrolyte respectively. For simplicity, cells based on

these electrolytes are forthwith referred to as 6µm-ScYSZ and 13µm-ScYSZ respectively and the *in-operando* cell described in section 2.2 denoted 13µm-ScYSZ-op.

Since it is difficult to quantify the effect of the alumina paste and Pt collectors surrounding half of the *in-operando* cell, we consider the active region of the cell the zone that is exposed to the open air. With this consideration the average current density is estimated to be 1.0 ±0.2 A/cm^2, which is on the order of current densities necessary to initiate void formation reported in the literature (2) (5).

Two representative examples of void formation on cleaved grain boundaries are shown in Figure 2 for the 13 and 6 µm grain size electrolytes. The structures have a similar appearance as to those reported in the literature, where the void size ranges from a few to approximately 100 nm (5) (24) (4). For comparison, a sample subjected to 850 °C for 72 hours with no potential difference between electrodes was taken as a reference showing no void formation. A representative image is shown in Figure S3 a) in Supplementary Material. Moreover, no void formation was found in any of the cathode/electrolyte interfaces of the samples subjected to a polarization of 2 V, a representative image is shown in Figure S3 b) in Supplementary Material.

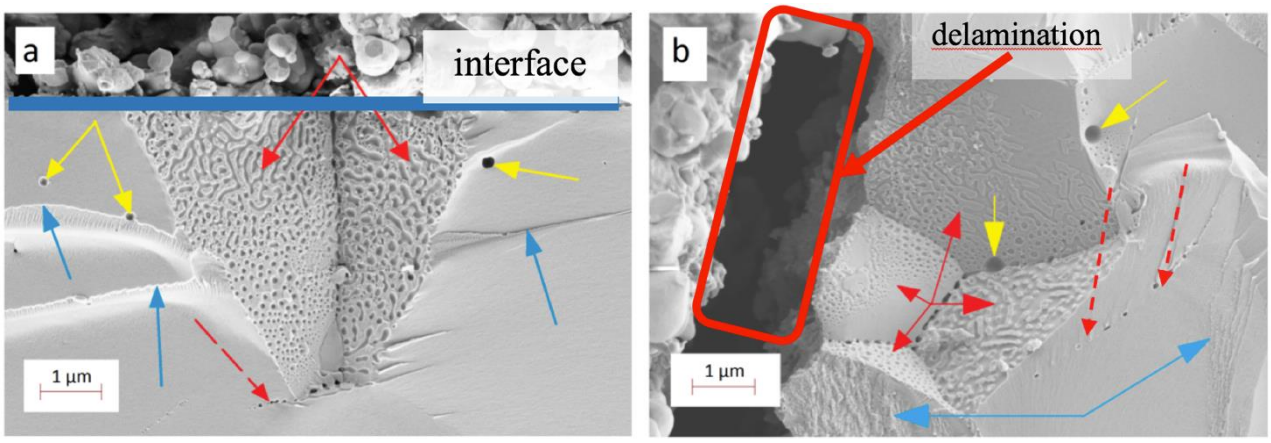

Figure 2. Examples of void formation indicated by red arrows, mainly in the grain boundaries of a) 13µm-ScYSZ at 900 °C for 12 hours and b) 6µm-ScYSZ at 900 °C for 72 hours. The anode/electrolyte interface in a) is indicated by the horizontal blue line and a delamination of the anode can be observed in b) indicated by the red box. Blue arrows indicate intra-grain structures when fracturing the sample, yellow arrows indicate intrinsic pinholes and dashed red arrows indicate void formation that could possibly be on a plane non-parallel to the fractured surface.

Regions pointed out by blue arrows in Figure 2 indicate surfaces where the fracture surface passes through grain interiors (intra-granular fracture) during the sample preparation. These fracture

surfaces contain features typical of fracture in low toughness materials. No extended surface areas of void formation were found in these regions, only lines of voids (dashed red arrows) were observed. These, "pearl-on-a-string" voids decorate grain boundaries oriented approximately orthogonal to the SEM images and represent a cross-section of the void patterns indicated by the red arrows on cleaved grain boundaries. Extensive void formation indicated by the red arrows corresponds to regions where the fracture path has followed grain boundaries weakened by void formation. Yellow arrows correspond to pre-existing pinholes and are identified by different characteristics compared to void clusters. For example, pinholes were observed randomly inside grains and on grain boundaries, their size, in many cases is significantly larger than the observed voids and are more isolated in a similar manner to untested material.

Void formation was also observed adjacent to edges of pinholes and at intragranular cracks, as observed in Figure 3. Also in typical surveyed images, with pixel size of 10 nm, the smallest individual voids that can be distinguished are estimated to be between 20-30 nm, however, occurrences of voids were only quantified when observed as an agglomeration of voids. Isolated voids were not considered significant. An example of the smallest voids is shown in Figure S4. These observations of voids close to pinholes, cracks and in the majority of the cases on grain boundaries may suggest that these defects can act as nucleation sites for voids.

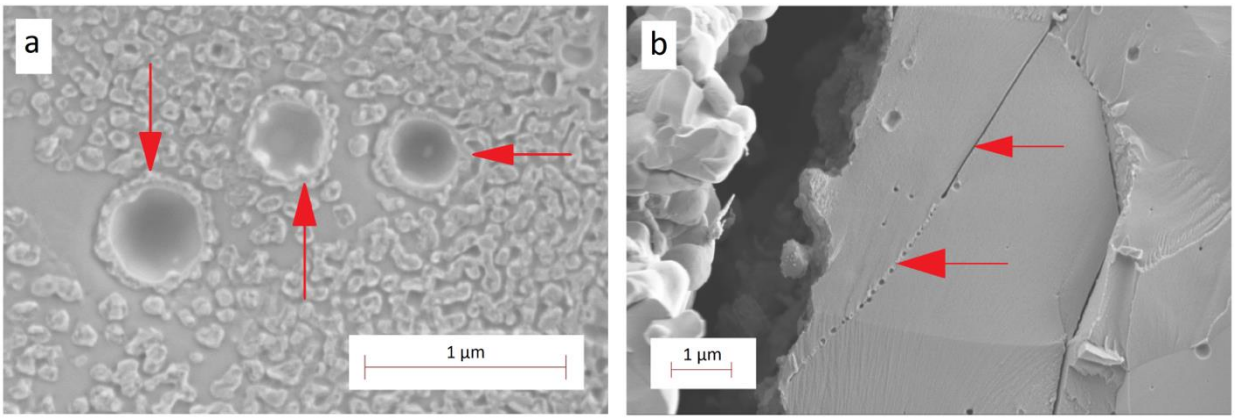

Figure 3. Void formation found in 6µm-ScYSZ at 900 °C for 72 hours a) surrounding intrinsic pinholes and b) continuing a crack in the electrolyte material, indicated by the red arrows.

3.1. Cavity formation close to the anode/electrolyte interface

Figure 4 shows the results of the SEM analysis of the void statistics experiments in terms of the ratio between the number of images with observed void formation and the total images along the interface for each case (denoted in the figure as the ratio of images), and their maximum observed electrolyte depth below the anode/electrolyte interface at different test durations and temperatures.

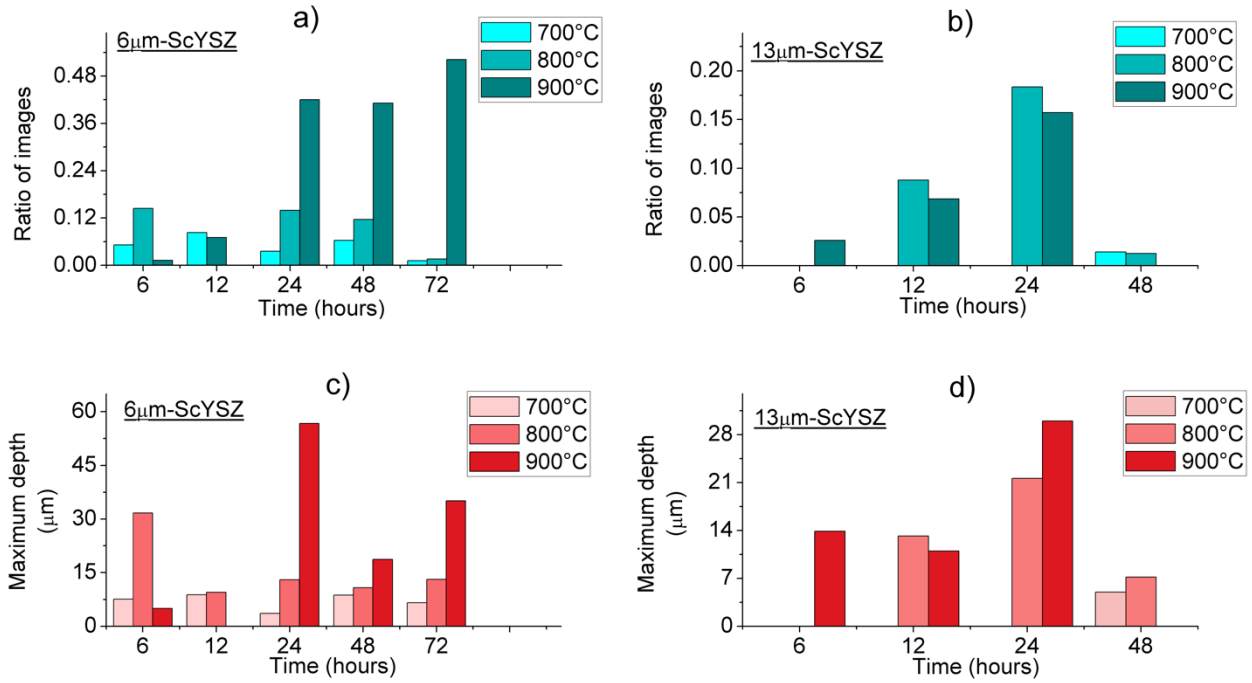

Figure 4. Statistics of void formation in ScYSZ. Column bars in a) and b) indicate the ratio of images where the void formation was observed for 6µm-ScYSZ and 13µm-ScYSZ respectively. Column bars in c) and d) indicate the maximum depth at which voids were found below the anode/electrolyte interface.

Note that the cells were tested in the full range of temperatures and durations. Therefore, a missing bar indicates a tested cell where no images containing void formation were recorded. In the cases with most occurrences, the ratio of images with voids is close to 50%, so void formation should not be considered a rare event in general.

As shown in Figure 4 a) for 6µm-ScYSZ cavity formation was observed after all tests and temperatures, with exceptions of 900 °C for 12 hours. In the cells subjected to an applied potential for 24 to 72 hours the occurrences of void formation, in general, increases with the temperature at each equivalent time. Only at 72 hours, the ratio of images remains practically the same at 700 and 800 °C, but then increases at 900 °C to a value consistent to what is observed at 24 and 48 hours. No clear trend was observed in this case for different operando times at the same temperature. A different scenario is observed in the case of the 13µm-ScYSZ cells, in Figure 4 b) where it appears that the larger grain size delays the onset of void formation at the lowest temperature of 700 °C. From Figure 4 it can be seen that statistics derived from quantifying void formation under optimized imaging conditions is limited by the stochastic nature of fracture surfaces between samples.

In Figure 4 c) for 6µm-ScYSZ the maximum depth where voids were found below the anode/electrolyte interface shows an increase with temperature at each equivalent time: 24, 48 and 72 hours, while no clear relation is observed at 6 and 12 hours. In Figure 4 d) there is no observable correlation for 13µm-ScYSZ regarding time and maximum depth in the cells; discussion of the observed poorer statistics of this case, compared to 6µm-ScYSZ, is given later.

It also should be noted that the detection of voids by SEM is dependent on the local fracture path during *post-mortem* sample preparation and the lack of detection is not necessarily an absolute verification of absence of cavities. Several inconsistencies in the trends of number of images and maximum observed depth can be observed in Figure 4. We attribute this scatter to hidden variables. Although great care was taken in following the same protocol by the same person for testing and sample preparation, some variables such as slight differences in the fracturing method could have affected some of the observations. This means that the confidence level in reporting the presence of void formation is significantly higher than in reporting its absence. More work is necessary in order to improve statistics of void observation and thus determine more rigorously the presence/absence of void formation and more reliable incubation periods. An alternative method to quantify void formation is to examine the cross-section of samples after mechanical polishing. Measuring microstructural features on polished planar cross-sections provides stereologically correct quantification features (25), in our case void number density per cubic micrometer. However due to the scale of the voids it is our experience that mechanical polishing obscures the majority of voids due to mechanical damage.

3.2. In-operando study of grain-averaged electrolyte lattice parameter change

In Figure 5 the evolution of the average d-spacing is shown as a function of depth from the positive electrode, with reference to the cell at 700 °C and no applied voltage (black horizontal line at 0 relative d-spacing). The various lines represent the different combinations of applied voltage and electrochemical operation time. The location of the vertical dash-dotted lines delimit the anode and cathode / electrolyte interfaces as determined by the number of diffraction spots on the detector as the 17 µm FWHM line beam was scanned across the cell edge. The complete graph, including standard deviations of the d-spacings and absolute d-spacing is shown in Figure S5 of supplementary material.

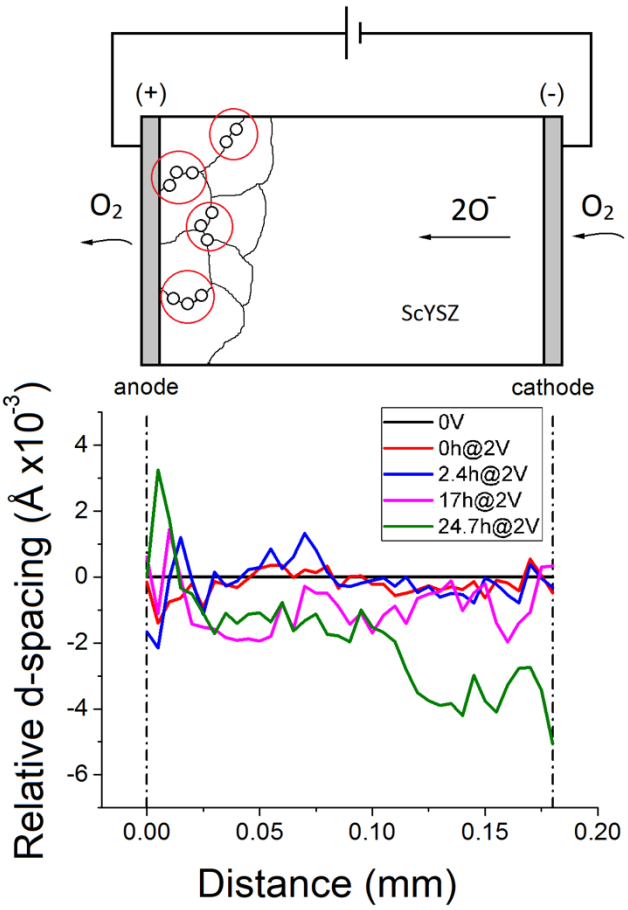

Figure 5. In-operando study. Top: a schematic view of the electrochemical cell setup with the expected oxygen void formation close to the anode. Irregular black lines and small black circles are representations of grain boundaries and void formation, marked with red circles. Bottom: evolution of d-spacing as a function of distance from the positive electrode relative to the reference condition, at 700 °C and 0 V (black horizontal line).

Within statistical uncertainty, there is no immediate change in d-spacing when applying the voltage, as evidenced by the black and red lines in Figure 5. The d-spacing did not change significantly during the first 2.4 hours either, see blue line. After 17 hours a decrease of d-spacing in the order of 1-2 $x10^{-3}$ Å, relative to the previous stage, was observed in the region from the electrolyte/anode interface to the middle of the electrolyte. However, an even more distinct change in d-spacing was observed at 24 hours, see green line, with a strong decrease of d-spacing towards the cathode/electrolyte region in the order of 4 $x10^{-3}$ Å. The fluctuations within the first 0.015 mm of the electrolyte from both electrode/electrolyte interfaces can be attributed to the geometry of the

cell, the beam width, and a relatively poor grain statistic. A more stable behavior was observed close to the cathode/electrolyte interface.

3.3. In-operando mapping of the strain evolution within a ScYSZ grain

To investigate the feasibility of mapping changes in the internal strain within a grain during cell operation, one average sized grain was selected and subjected to dark field microscopy at regular intervals during the annealing in the *in-operando* experiment. This grain was located less than 25 µm from the anode/electrolyte interface. By combined translation/rotation of the objective and a translation of the detector (see Figure 1) we effectively scanned the scattering angle 2θ around its nominal position of 14.186° within a range of ± 0.05°. In this way, maps of the axial strain were provided (22). These maps are 2D projections of the grain, as the beam height is larger than the grain size. Shown in Figure 6 are strain maps acquired initially – at room temperature – and after 10.5 hours of operation at 2V.

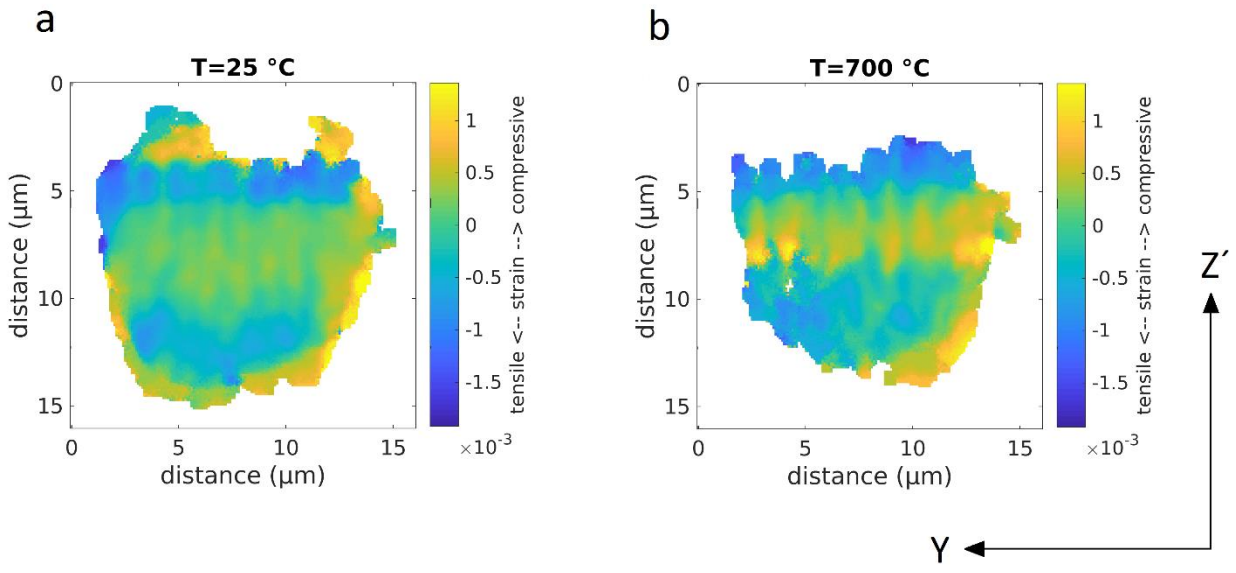

Figure 6. Strain maps of a single grain close to the anode/electrolyte interface. Positive and negative values imply compressive and tensile strain respectively. a) Grain at room temperature and no applied voltage. b) The same grain at 700 °C and 2V polarization after 10.5 hours at operating conditions. The anode/electrolyte interface is above the image. The "y" axis is defined in ***Error! Reference source not found.*** *while the z´ -axis represents the axis perpendicular to the 2θ direction and the "y" axis. The pixel size is 0.1 µm and the color bars have the same scale.*

At initial conditions, regions with compressive strain in the order of $1x10^{-3}$ and larger are localized mostly close to the grain exterior. Regions with strain between $0.5x10^{-3}$ and $-0.5x10^{-3}$ are distributed inside the grain. After 10.5 hours, an increase of local compressive strain in the central regions from approximately $0.7x10^{-3}$ to more than $1x10^{-3}$ is observed.

3.4. Characterization of grain boundary void formation after operation

A *post-mortem* analysis of the 13µm-ScYSZ-op cell by SEM is shown in Figure 7. It reveals void formation in the grain boundaries of the electrolyte close to the anode/electrolyte interface. These appear at a maximum depth into the electrolyte from the anode/electrolyte interface of approximately 10 µm, similar to the range observed in the 13µm-ScYSZ *post-mortem* sample as shown in Figure 4.

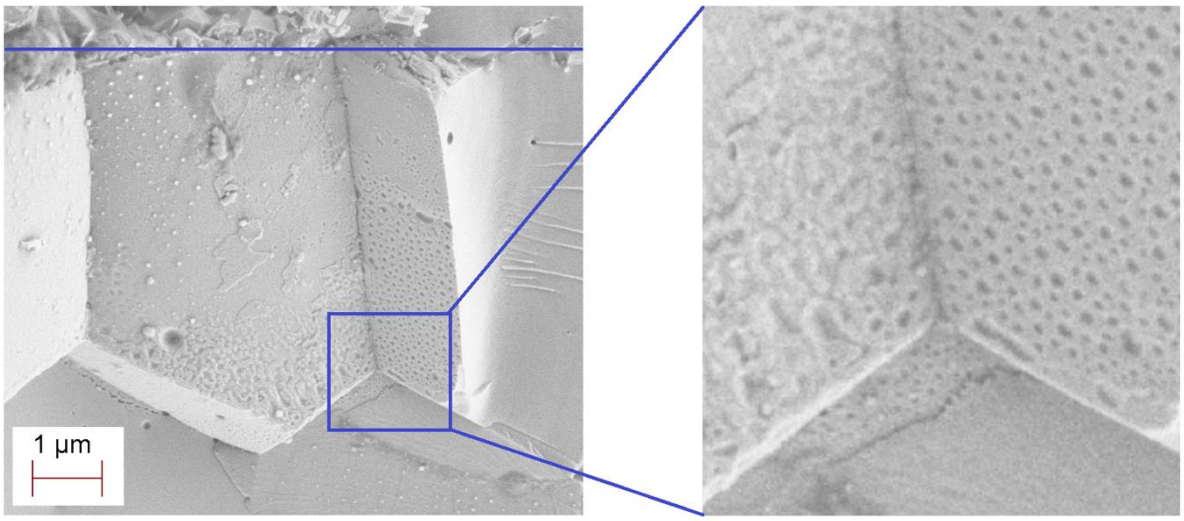

Figure 7. SEM micrographs of the fractured 13µm-ScYSZ-op revealing void formation in the electrolyte near the anode/electrolyte interface. The blue horizontal line marks the interface between electrolyte (below) and anode (above). To the right a 4.2X magnified image of the area indicated by the blue box is shown.

4. Discussion

4.1. Conditions and factors influencing void formation

The present work, as illustrated in Figure 4 shows that under realistic operating conditions at high polarization, electrolyte grain boundary void formation onset commences within a few hours and is relatively independent of typical operation temperatures. In the case of 6µm-ScYSZ the incubation period appears to be shorter than 6 hours at all three temperatures. The presence/absence of void

formation for 13µm-ScYSZ, in comparison to 6µm-ScYSZ where voids are present for all conditions, suggests that the grain size has an effect on the incubation period, as there appears to be a great absence of voids at the lower temperatures. An analogous hypothesis of an incubation period is also supported by Graves et al. (2), in which a YSZ cell with Ni-YSZ and LSM/YSZ as fuel and oxygen electrodes respectively was reversibly tested at 800°C, in cycles of electrolysis and fuel cell mode every 5 hours each under a current density of -1/+0.5 A/cm^2 respectively. This treatment limited the cell voltage to 1.33 V in electrolysis mode in comparison to a cell run at equivalent electrolysis conditions where the cell voltage climbed steadily to 1.73V in over 400 h. No significant degradation occurred in cycling mode, with no void observation after hundreds of hours of test. For the cell at constant current, void formation was observed under continual electrolysis operation after reaching high values of cell potential. This suggests that an incubation period exists in which the critical level of high internal oxygen pressure is not reached and oxygen pore formation can be avoided by maintaining a low cell voltage. Alternatively, if void formation occurs, it is hypothesized by Graves et al. (2) that in the fuel cell mode voids can be removed by pumping the oxygen, when the pO_2 is lowered. However, no microstructural evidence is provided establishing that either void formation occurs continuously with increasing cell voltage or that a limiting cell voltage for void formation initiation exists. Furthermore, no evidence exists to our knowledge that once a void is formed for a given cell voltage that void can be removed again.

To our knowledge, void formation has previously only been reported for YSZ (5) (2) (4). The present work reveals that void formation occurs under similar operating conditions and with a similar morphology in ScYSZ. Moreover, the incubation time is shown to be as short as 6 hours, comparable to what was observed by Graves et al. (2). Consistent void formation in both these materials thus suggests that the stabilizing dopant Y_2O_3 / Sc_2O_3 does not have a significant effect on void formation.

The higher occurrence of void observations in 6µm-ScYSZ in comparison to 13µm-ScYSZ in the addressed temperature and time range may suggest a dependence of this effect on the grain size, and thus the grain boundary specific interface area. This, in addition to the observation of voids close to pinholes and cracks, may suggest that reducing and/or eliminating these defects and reducing the grain boundary interface area could be a mitigation mechanism to reduce the nano-sized void formation, thus increasing the lifetime of the cell.

Void formation is believed to be caused by a build-up of oxygen pressure due to the distribution of electrochemical potential inside the electrolyte (4) (5) (7). Kim et al. (26) suggested that the detected presence of La, Sr and Mn impurities along the grain boundaries of YSZ could be considered as a sink to release electrons from the oxide ions, where oxygen gas builds up, thus

resulting in high oxygen gas pressure at grain boundaries and intergranular fracture. However, diffusion of these elements into the ScYSZ was not detected in our case, based on analyses by energy-dispersive X-ray spectroscopy.

4.2. Microstructural changes close to the anode/electrolyte interface

As shown in Figure 7, the *in-operando* cell 13µm-ScYSZ-op, shows void formation after 32 hours. As we evidently have no similar analysis at shorter times, we cannot prove the existence of void formation at earlier times. However, the decrease of d-spacing at 17h@V and 24.7h@V (see Figure 5) indicates an increase of compressive stress at the anode side. Assuming that all changes in lattice parameter are stress induced, using a Young´s Modulus of 158 GPa for 6mol%ScYSZ at 700 °C (27), the axial stress is up to 100 MPa within the first 100 µm of the electrolyte for the 24.7 hour case (see also Figure S6 in supplementary material). This value of stress estimated above is one order of magnitude larger than the 10 MPa predicted by Virkar et al. (9) to be sufficient to cause delamination of the anode, although no void formation is mentioned in that study. In the present study both delamination and voids were observed only in the SEM images related to the most extreme case: 6µm-ScYSZ at 900 °C for 72 hours. Analogous delamination have been observed by Chen et al. (28) in cells composed by LSM electrodes and YSZ electrolyte under current densities of 0.5 A/cm^2 in electrolysis mode at 800 °C in air, with an increase of anodic polarization potential from 1.12 to 1.73 V, where a proposed mechanism of this effect is also described.

The maximum depth at which voids were detected in this cell was approximately 13 µm. Considering the uncertainty of the d-spacing near the anode/electrolyte interface and the validity of the assumption above we are unable to establish an explicit correlation between the void formation depth and stress magnitude.

4.2.1. Local strain within a grain

The unique x-ray microscopy results presented in Figure 6 demonstrate the feasibility of in operando mapping of the individual grains. The increase of local strain areas in Figure 6 b) is consistent with an increase of the overall strain of the grains close to the anode/electrolyte interface as evidenced by Figure 5. We interpret the changes between the left and the right figure as indicative of strain localization at the grain boundaries: the pre-cursor of the pore formation. More specifically:

- The morphology of the grain projection is not the same in the two maps in Figure 6. In particular, some areas are missing in the outer parts of the treated grain where these locations no longer locally meet the Bragg condition. This indicates that these zones either

experience: a) local crystal rotation greater than the ±0.05° rotation in rocking angle performed during each scan and/or b) extremely high axial strain corresponding to variations in the lattice parameter of $\Delta 2\theta > 0.05°$, i.e. on the order of $\pm 35 \times 10^{-3}$ or larger. However, elastic axial strains at these extremes are unlikely as they correspond to stresses on the order of 5 GPa and would thus either result in fracture, or local lattice rotation consistent with a). In other words, regions at the grain boundaries are experiencing significant local deformation. Kim et al. (26) reported complete separation of grain regions as intergranular cracks in a YSZ electrolyte operated at 750 °C for 120 hours in air under high current density. It should be noted that the outer shape of the grain and values of inner strain may be influenced by the chosen level of background intensity, which is selected visually by setting a suitable value to remove single and weak pixels without removing what appears to be the grain. However, in our case the same procedure is applied in both images.

- The horizontal band with nearly regularly spaced yellow vertical intensity ridges appearing in Figure 6b may indicate an array of hot spots appearing at the top or bottom surface of the grain investigated. Notably the local strain would be substantially larger than the 10^{-3} indicated, as the figure is a projection over the entire grain.

4.3. d-spacing decrease close to the cathode/electrolyte interface

The observed decrease in d-spacing near the cathode side of the electrolyte at 24.7 hours at operating conditions is an unexpected result and presently there are no definitive mechanisms available to explain this phenomenon. A rigorous investigation for sources of experimental artefacts that could replicate this observation was performed. The relevant sources of error are associated with sample or detector drift during the course of the 24-hour scan. Investigation of potential drifts for each detector/sample coordinate axis however proved to be internally consistent. It was thus concluded, within the resolution limits, that the potential artefacts do not explain the magnitude of the observed change in lattice parameter in Figure 5.

We speculate that the effect of d-spacing decreasing may be related to an increase in oxygen vacancy concentration close to the cathode region and/or the cathode itself. Studies have revealed a decrease in the unit cell volume of oxygen-deficient ZrO_2 when firing and quenching it at high temperature (29). It is suggested that the decrease of lattice parameter is due to oxygen missing and not from additional Zr in the structure. More recently, Marrocchelli et al. (30) concluded that oxygen vacancy formation results in a decrease of lattice parameter due to electrostatic interactions in computer simulations with ZrO_2.

If the oxygen reduction rate at the cathode/electrolyte interface is limited, insufficient oxide ions will be supplied via the electrolyte to the anode. In this case, it is reasonable to assume that oxygen from the ScYSZ lattice can be extracted in order to maintain the electrochemical reaction, promoting an oxygen deficiency in the structure close to the cathode. Causes for oxygen deficiency could be potentially related to the following mechanisms: a decrease in TPB length due to coarsening of LSM phase (31), oxygen depletion due to gas diffusion limitation in the LSM cathode (32) or partial delamination and/or microcracks at the cathode/electrolyte interface.

This oxygen deficiency or increase in oxygen vacancy concentration close to the cathode may explain the large decrease of d-spacing after 24.7 hours under operating conditions when combined with the aforementioned negative chemical expansion coefficient. In addition, the negligible d-spacing change at 17h@V in comparison to 0h@V close to the cathode/electrolyte interface region may indicate a threshold time in which oxygen vacancy concentration starts to increase, shown in the right side of the plot in Figure 5.

4.4. Instrumental outlook

A strength of the set-up used is the ability to swap between strain mapping at the scale of the device (Figure 5) and dark field microscopy at the scale of a grain (Figure 6). With the ad hoc set up used at the time of this experiment, the scans in Figure 5 took 70 minutes while the microscopy scans took approximately 16 minutes. However, periodically relocating the same grain in reciprocal and real space and finding new grains took several hours, which is not convenient in a beamtime period of a few days. Since the experiment, a dedicated instrument has been commissioned and the time for alignment is much reduced. Hence, it is now realistic to perform dark field microscopy on several grains interchangeably during an annealing, thus improving statistics and insight.

Furthermore, with the upgrade of ESRF to become an ultimate storage ring in 2020, we anticipate that scan times can be reduced by an order of magnitude. This will make it feasible to reduce the height of the incoming beam to say 1 μm, and to scan the grain of interest with respect to the beam. In this way, one would replace 2D projections of a grain – as shown in Figure 6 - with a real 3D grain map.

5. Conclusions

Solid oxide cells are organized structurally on multiple length scales. To understand degradation mechanisms and verify materials models it is of interest to develop *non-destructive* tools for multiscale structural characterization, enabling to zoom in and out in 3D in an actual device during

an experiment. To our knowledge, this study is the first demonstration of such a tool. Two novel synchrotron methods are combined for use on SOCs. On the device scale, classical x-ray powder diffraction is replaced by strain mapping using multigrain crystallography methods, in order to overcome the problem of grain statistics. On the grain scale, we introduce dark field x-ray microscopy. Targeting the question of void formation and delamination during operation at high polarization, the x-ray methods are combined with extensive SEM post mortem studies.

The ScYSZ electrolyte based cells were tested at 700, 800 and 900 °C during 6 to 72 hours of operation at 2 V in air. For the first time void formation was shown to form as early as 6 hours in ScYSZ. These appeared at the grain boundaries close to the anode/electrolyte interface and also surrounding pinholes. For 6μm-ScYSZ correlations were found for void occurrences and maximum observed depth with increasing temperature at equivalent operando times between 24 and 72 hours.

The x-ray studies provide a coherent picture of the degradation mechanism taking place within the electrolyte near the anode/electrolyte interface. Within the grains, dark field X-ray microscopy showed an increase in local compressive strain inside the projection of the grain and rotated regions at the edges after 10.5 hours - both consistent with strain localization at the boundary of the grain. After 17 hours this phenomenon is evident as an increase in the grain average axial strain in a 100 μm region near the interface. Thus void formation, as evidenced by the post mortem SEM study, leads to lattice strain.

An unexpected decrease of electrolyte d-spacing close to the cathode interface was observed and is tentatively associated to an increase of oxygen vacancy concentration in this region due to oxygen deficiency caused by degradation factors occurring at the cathode. Further investigations need to be made in order to elucidate the responsible mechanism.

Acknowledgements

The authors would like to thank ESRF for granting the beamtime and DTU DANCHIP for manufacturing the X-ray condenser lenses used at beamline ID06. We also acknowledge financial support from the ERC Advanced Grant, d-TXM and travel support for synchrotron experiments via the DANSCATT grant from the Danish Council for Independent Research. We thank Sonja R. Ahl, Karin V. Hansen, Torben Jacobsen, Mogens B. Mogensen, Ming Chen, Christodoulos Chatzichristodoulou and Bhaskar Reddy for stimulating discussions; and technicians at DTU Energy: E. Abdellahi, A. Mikkelsen and J. Johnson for their support on sample preparation and experiments. We also thank Innokenty Kantor for his support during beamtime.

6. Bibliography

1. *Solid Oxide Fuel Cell Technology.* **Huang, K. and Goodenough, J. B.** 2009, Woodhead Publishing.

2. *Eliminating degradation in solid oxide electrochemical cells by reverisble operation.* **Graves, C., et al.** 2014, Nature Materials, pp. 239-244.

3. *High Temperature Electrolysis in Alkaline Cells, Solid Proton Conducting Cells, and Solid Oxide Cells.* **Ebbesen, S. D., et al.** 2014, American Chemical Society, pp. 10697-10734.

4. *Solid Oxide Electrolysis Cells: Degradation at High Current Densities.* **Knibbe, R., et al.** 2010, Journal of The Electrochemical Society, pp. 1209-1217.

5. *Degradation phenomena in a solid oxide electrolysis cell after 9000 h of operation.* **Tietz, F., et al.** 2013, Journal of Power Sources, pp. 129-135.

6. *Durability of Solid Oxide Electrolysis Cell and Interconnects for Steam Electrolysis.* **Sun, X., et al.** 1, 2013, The Electrochemical Society, Vol. 57, pp. 3229-3238.

7. *The Course of Oxygen Partial Pressure and Electric Potentials across an Oxide Electrolyte Cell.* **Jacobsen, T. and Mogensen, M.** 2008, The Electrochemical Society, pp. 259-273.

8. *Understanding degradation of solid oxide electrolysis cells through modeling of electrochemical potential profiles.* **Chatzichristodoulou, C., et al.** 2016, Electrochimica Acta, pp. 265-282.

9. *Mechanism of oxygen electrode delamination in solid oxide electrolyzer cells.* **Virkar, A. V.** s.l. : Elsevier Ltd, 2010, International Journal of Hydrogen Energy, Vol. 35, pp. 9527-9543.

10. *Oxygen permeation flux through 10Sc1YSZ-MnCo2O4 asymmetric membranes prepared by two-step sintering.* **Pirou, S., et al.** 2016, Fuel Processing Technology, Vol. 152, pp. 192-199.

11. *Analysis of Electric Properties of ZrO2–Y2O3 Single Crystals Using Teraherz IR and Impedance Spectroscopy Techniques1.* **Artemov, V. G., et al.** 7, 2014, Russian Journal of Electrochemistry,, Vol. 50, pp. 690-693.

12. *Preparation of Yttria-Stabilized Zirconia by the Reverse Microemulsion Method and the Effect of Sc and Ce Doping on Microstructure and Ionic Conductivity for Solid Oxide Fuel Cell Applications.* **Oksuzomer, F., et al.** 2011, International Journal of Applied Ceramic Technology, pp. 42-48.

13. *Investigation of scandia–yttria–zirconia system as an electrolyte material for intermediate temperature fuel cells - influence of yttria content in system (Y2O3)x (Sc2O3)(11-x) (ZrO2)89.* **Politova, T. I. and Irvine, J. T. S.** 2004, Solid State Ionics, pp. 153-165.

14. *Co-doping of scandia–zirconia electrolytes for SOFCs.* **Irvine, J. T. S., et al.** 2006, The Royal Society of Chemistry, Vol. 134, pp. 41-49.

15. *Dark-field X-ray microscopy for multiscale structural characterization.* **Simons, H., et al.** 2015, Nature Communications, pp. 1-6.

16. *Multiscale 3D characterization with dark-field x-ray microscopy.* **Simons, H., et al.** 2016, MRS Bulletin, Vol. 4, pp. 454-459.

17. *Influence of oxygen partial pressure on surface tension of molten silver.* **Ozawa, S., et al.** 2010, Journal of Applied Physics, Vol. 107, pp. 014910-1 - 014910-7.

18. *YSZ-Based Oxygen Sensors and the Use of Nanomaterials: A Review from Classical Models to Current Trends.* **Lopez, C., Ramos, F. M. and Cirera, A.** 2009, Journal of Sensors, Vol. 2009, p. 15.

19. *Three-Dimensional X-Ray Diffraction Microscopy - Mapping Polycrystals and their Dynamics.* **Poulsen, H. F.** 2004, Springer, Vol. 205.

20. *Tutorial and source code of ImageD11.* **Wright, J.** s.l. : sourceforge, https://github.com/jonwright/ImageD11.

21. *X-ray diffraction microscopy based on refractive optics.* **Poulsen, H. F., et al.** 2017, Journal of Applied Crystallography, Vol. 50, pp. 1441-1456.

22. *Dark field X-ray microscopy for studies of recrystallization.* **Ahl, S. R., et al.** 2015, Materials Science and Engineering.

23. *Average Grain Size in Polycrystalline Ceramics.* **Mendelson, M. I.** 1969, Journal of the American Ceramic Society, pp. 443-446.

24. *Electrolyte degradation in anode supported microtubular yttria stabilized zirconia-based solid oxide steam electrolysis cells at high voltages of operation.* **Laguna-Bercero, M. A., et al.** 2011, Journal of Power Sources, pp. 8942-8947.

25. *Quantitative Stereology.* **Underwood, E. E.** 1970, Addison-Wesley.

26. *Degradation mechanism of electrolyte and air electrode in.* **Kim, J., et al.** 2013, International Journal of Hydrogen Energy, pp. 1225-1235.

27. *High temperature mechanical properties of zirconia tapes used for electrolyte supported solid oxide fuel cells.* **Fleischhauer, F., et al.** 2015, Journal of Power Sources, Vol. 273, pp. 237-243.

28. *Failure mechanism of (La Sr) MnO3 oxygen electrodes of solid oxide electrolysis cells.* **Chen, K. and Jiang, S. P.** 36, 2011, International Journal of Hydrogen Energy, pp. 10541-10549.

29. *Nonstoichiometry of ZrO2 and its relation to tetragonal-cubic invesrion in ZrO2.* **Ruh, R. and Garret, H. J.** 5, 1967, Journal of the American Ceramic Society, Vol. 50, pp. 257-261.

30. *Understanding Chemical Expansion in Non-Stoichiometric Oxides: Ceria and Zirconia Case Studies.* **Marrocchelli, D., et al.** 2012, Advanced Functional Materials, Vol. 22, pp. 1958–1965.

31. *Particle Coarsening Influence on Oxygen Reduction in LSM-YSZ composite Materials.* **Farlenkov, A. S., et al.** 1, 2015, Fuel Cells, Vol. 15, pp. 131-139.

32. *Impedance of Solid Oxide Fuel Cell LSM/YSZ Composite Cathodes.* **Jørgensen, M. J. and Mogensen, M.** 5, 2001, Journal of The Electrochemical Society, Vol. 148, pp. A433-A442.